Localized Electrons Enhanced Ion Transport for Ultrafast Electrochemical Energy Storage

Jiewei Chen, Bi Luo, Qiushui Chen, Fei Li, Yanjiao Guo, Tom Wu, Peng Peng, Xian Qin, Gaoxiang Wu, Mengqi Cui, Lehao Liu, Lihua Chu, Bing Jiang, Yingfeng Li, Xueqing Gong, Yang Chai, Yongping Yang, Yonghua Chen, Wei Huang, Xiaogang Liu,* and Meicheng Li*

The rate-determining process for electrochemical energy storage is largely determined by ion transport occurring in the electrode materials. Apart from decreasing the distance of ion diffusion, the enhancement of ionic mobility is crucial for ion transport. Here, a localized electron enhanced ion transport mechanism to promote ion mobility for ultrafast energy storage is proposed. Theoretical calculations and analysis reveal that highly localized electrons can be induced by intrinsic defects, and the migration barrier of ions can be obviously reduced. Consistently, experiment results reveal that this mechanism leads to an enhancement of Li/Na ion diffusivity by two orders of magnitude. At high mass loading of 10 mg cm^{-2} and high rate of 10C, a reversible energy storage capacity up to 190 mAh g^{-1} is achieved, which is ten times greater than achievable by commercial crystals with comparable dimensions.

Electrochemical energy storage devices such as Li-ion batteries (LIBs), Na-ion batteries (NIBs), supercapacitors, and fuel cells, have been widely investigated because of their practical utility for applications in mobile electronics, electric vehicles, and renewable energy industry.[1–6] The performance of these energy storage devices largely relies on the rate of charge (electrons and ions) transport, especially within electrode materials.[7,8] To achieve high-rate storage at practical levels of mass loading ($\approx$10 mg cm^{-2}), it is particularly important to promote the mass transport of ions to an optimized high rate because insufficient ion transport could seriously reduce the capacity and rate of the energy storage devices.[2–4,9,10]

Recently, tremendous progress has been made in improving the ion transport through the size and morphological control to shorten the ion transport distance in the electrode materials. A general strategy is to synthesize nanocrystals and use them as the electrode materials.[10] Alternatively, the construction of hierarchical structures with contact surfaces easily accessible between electrode materials and electrolyte is another feasible approach.[11,12] For example, ions can easily diffuse into 3D holey-graphene architectures to render high-rate energy storage.[13] Notably, controlling ionic mobility in the electrode material, particularly for electrodes of high mass loading, is another important factor for enhanced energy storage.[2,12] Despite enormous efforts, there are relatively few

J. Chen, B. Luo, Y. Guo, P. Peng, G. Wu, M. Cui, Dr. L. Liu, Dr. L. Chu, Dr. B. Jiang, Dr. Y. Li, Prof. Y. Yang, Prof. M. Li
State Key Laboratory of Alternate Electrical Power System
with Renewable Energy Sources
North China Electric Power University
Beijing 102206, China
E-mail: mcli@ncepu.edu.cn
Dr. Q. Chen, Dr. X. Qin, Prof. X. Liu
Department of Chemistry
National University of Singapore
Singapore 117543, Singapore
E-mail: chmlx@nus.edu.sg
F. Li, Prof. X. Gong
Key Laboratory for Advanced Materials
Centre for Computational Chemistry and Research Institute
of Industrial Catalysis
School of Chemistry and Molecular Engineering
East China University of Science and Technology
Shanghai 200237, China

Prof. T. Wu
School of Materials Science and Engineering
University of New South Wales
Sydney, NSW 2052, Australia
Prof. Y. Chai
Department of Applied Physics
The Hong Kong Polytechnic University
Hung Hom, Kowloon, Hong Kong 999077, China
Prof. Y. Chen, Prof. W. Huang
Key Laboratory of Flexible Electronics (KLOFE) and Institute
of Advanced Materials (IAM)
Jiangsu National Synergetic Innovation Center for Advanced
Materials (SICAM)
Nanjing Tech University
Nanjing 210028, China
Prof. W. Huang
Shaanxi Institute of Flexible Electronics (SIFE)
Northwestern Polytechnic University (NPU)
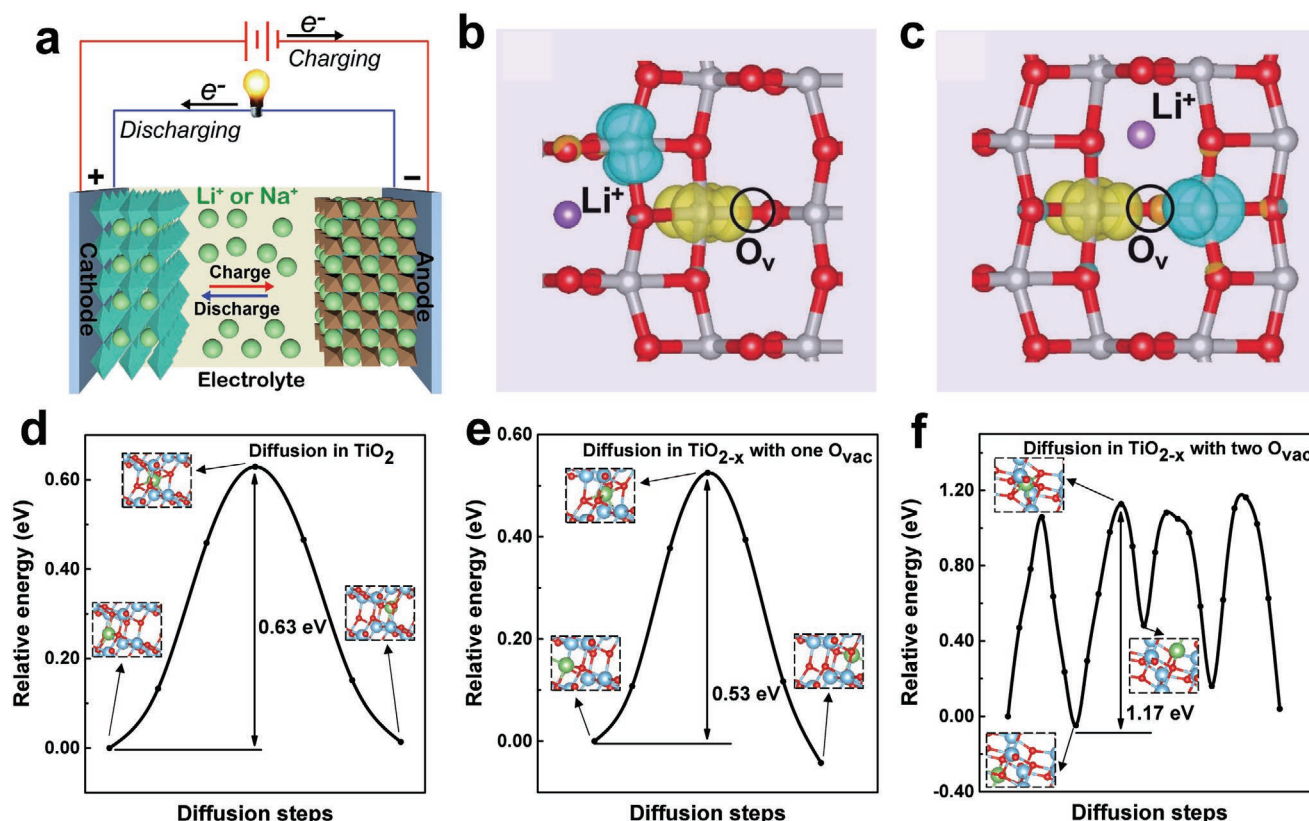Xi'an 710072, China

Figure 1. Mechanistic illustration of localized electrons enhanced ion transport for high-rate electrochemical energy storage. a) Schematic concept of localized electrons enhanced ion transport for efficient performance. The rate for charging and discharging process can be improved by speeding up ion diffusion in electrode materials of energy storage electrochemical devices. b,c) Calculated spin-polarized charge densities (isosurface level = 4×10^{-3} e$^-$ Å^{-3}) of oxygen-deficient TiO_2 (101) upon Li$^+$ migration to different locations. The yellow and blue colors mark the position of excess electrons, which are mainly located at specific Ti atoms. As the location of Li$^+$ changes, the localized electrons moves to the location near the Li$^+$, correspondingly. d–f) The energy profile of Li$^+$ migration along the diffusion pathway for perfect TiO_2 (0.63 eV), TiO_{2-x} with one vacancy (0.53 eV), and TiO_{2-x} with two neighboring oxygen vacancies (1.17 eV), respectively.

reports concerning the improvement of ion mobility of electrode materials for enhanced energy storage.

The nature of ion diffusion is dependent upon the atomic arrangement in electrode materials. The ion transport in a material is generally governed by two basic mechanisms: interstitial diffusion and vacancy diffusion, both of which have been widely used to interpret the phenomena of random ion transport in electrode materials.[7,8] Different from the conventional mechanism, it was reported that during the charging or discharging step, the ion transport can be strongly affected by the coupled interaction between the ions and movable electrons from exteriorly injecting.[14,15] Nowadays, however, there is still little study on how highly localized electrons inside the materials affect the ion transport. Such electrons can be introduced in defective materials instead of exteriorly injecting,[16–19] such as the localized excess electrons at Ti atoms near the oxygen vacancy in TiO_2.[16,20,21] We expect that the interaction between the ions and localized electrons can be harnessed to significantly improve the ion transport in electrode materials for enhanced energy storage.

To probe the intrinsic effect of highly localized electrons on ion transport, it is imperative to eliminate some other factors, such as volume expansion and solid electrolyte interphase

reaction during charging and discharging. Semiconductor TiO_2 is an ideal model material for such a study because the TiO_2 electrode materials, commonly used as a stable protective layer, only exhibit a volume expansion of less than 4% during charging/ discharging[22–25] and the localized electron formation due to unpaired electrons in defective TiO_2 has been extensively investigated.[26] We assume that the localized electrons are formed at the oxygen vacancy (V_o), where excess electrons are localized near Ti atoms.[21] **Figure 1**a shows the schematic concept of localized electrons enhanced ion transport through the use of TiO_2 with localized electrons as the anode. The rate for charging and discharging process can be improved by speeding up ion diffusion in electrode materials of energy storage electrochemical devices. As shown in Figure 1b,c, density functional theory (DFT) calculations were conducted to determine the spin-polarized charge densities (isosurface level = 4×10^{-3} e$^-$ Å^{-3}) of oxygen-deficient TiO_2 (101) upon Li$^+$ insertion. The yellow and blue colors denote the position of excess electrons, which are mainly located at specific Ti atoms. Such excess electrons can be treated as centers of negative charge for facile trapping of positive ions, especially alkaline ions, because there is only one valence electron in the alkaline atom.[27] Comparing Figure 1b,c, it visually shows that there exists the electrostatic

interaction between Li$^+$ and localized electrons because as the location of Li$^+$ changes, the localized electrons move to the location near the Li$^+$, correspondingly.

We took a further step and systematically investigated the distribution of excess electrons under different situations through calculations. At the surface of the anatase TiO$_2$ (101), the excess electrons are localized either at: i) nonequivalent Ti$_{5c}$/Ti$_{6c}$ sites, or ii) two neighboring Ti$_{5c}$ sites (Figure S1, Supporting Information). The corresponding oxygen vacancy formation energies (E_{vf}) were 3.53 eV for case (i) and 3.06 eV for case (ii), indicating that the latter is more stable. In addition, we investigated the effects of Li$^+$/Na$^+$ insertion on the distributions of excess electrons around Ti atoms (Figure S2, Supporting Information). We found that the excess electrons tend to localize at nonequivalent Ti$_{5c}$ and Ti$_{6c}$ sites when the Li$^+$/Na$^+$ ions are slightly distant from the oxygen vacancy (Figure S2a,b, Supporting Information), while the excess electrons tend to localize at two neighboring Ti$_{5c}$ sites when the Li$^+$/Na$^+$ ions are close to the oxygen vacancy (Figure S2c,d, Supporting Information). Different localization patterns of the excess electrons can be attributed to the attraction of Li$^+$/Na$^+$ ions.

We further investigated the distribution of the excess electrons in the bulk TiO$_2$ in the case of Li$^+$/ Na$^+$ insertion. We did not observe any notable change in the crystal structures of oxygen-deficient TiO$_2$ before and after Li$^+$/Na$^+$ insertion (Figure S3, Supporting Information). These results suggest that the excess electrons are likely localized at the neighboring three 5-fold coordinated Ti sites, denoted as Ti$_{5c}$ (Ti$_1$, Ti$_2$, and Ti$_3$) in the bulk TiO$_2$. Moreover, density of states (DOS) and partial density of states (PDOS) of oxygen-deficient bulk TiO$_2$ without and with the Li$^+$/Na$^+$ insertion revealed a gap state of about 1 eV below the bottom of the conduction band of oxygen-deficient TiO$_2$ (Figure S4, Supporting Information), which can be attributed to Ti^{3+}.[28–31] Overall, our DFT calculations supported the localized excess electrons associated with O vacancies.

Some works reported that the movable electrons injected from the external circuit can strongly affect the transport of ions.[14,15] Referring to these works, the localized electrons near the oxygen vacancy should also affect the ion transport. Here, the migration barriers of Li$^+$ in different configurations are investigated to reveal the effects of how localized electrons affect the transport of Li$^+$. The diffusion of Li$^+$ from one stable site to another one within the anatase TiO$_2$ slab is depicted in Figure S5a, Supporting Information, and the energy profile along the diffusion pathway is shown in Figure 1d. The active energy barrier on the pathway is calculated to be 0.63 eV, and the structure of Li$^+$ locating at the center of the smaller O$_6$ octahedral was identified as the transition state. Sequentially, we investigated the diffusion of Li$^+$ in the defective anatase TiO$_{2-x}$ with one oxygen vacancy (Figure S5b, Supporting Information). The diffusion capability of Li$^+$ is improved in the defective anatase TiO$_{2-x}$, as suggested by the energy profile (Figure 1e) with the energy barrier of 0.53 eV.

Different configuration strongly affects the migration barrier. For bulk oxygen vacancies, generally, there are two kinds of situations: 1) away from each other or 2) near each other. For situation (1), the interaction between different vacancies is relatively weak, and such situation can be taken as one oxygen in the configuration when Li$^+$ migrates. As for situation (2), Li$^+$ diffusion in the defective anatase TiO$_{2-x}$ with two neighboring oxygen vacancies, the energy profile (Figure 1f) along the pathway (Figure S5c, Supporting Information) indicates that Li$^+$ migrates in the defective anatase TiO$_{2-x}$ with two oxygen vacancies might be quite difficult because of the high energy barrier of 1.17 eV. The possibility of oxygen vacancies near each other can increase if there are too many bulk oxygen vacancies, which can obviously inhibit the Li$^+$ transport. Hence, there is optimized Ti^{3+} concentration for the Li$^+$ transport in order to achieve the best energy storage performance.

To reveal whether the electrostatic interaction between Li$^+$ and localized electrons play an important role in reducing the migration barrier under the extrinsic electrical field during charging/discharging, the electrical field is applied in the migration path. The result shows that Li$^+$ migration barrier decreases by about 0.16 eV in TiO$_{2-x}$ compared with the no electrical field situation. Thus, the extrinsic electrical field can strongly enhance the Li$^+$ migration when there are localized electrons near the migration path. Positive ions and localized negative electrons interaction model is used to help explain this phenomenon (Figure S6, Supporting Information).

Based on the localized electrons enhanced ion transport (LIT) mechanism revealed by our DFT calculations, we proposed a general approach to introducing localized electrons into electrode materials. In our work, oxygen-deficient TiO$_2$ materials were synthesized by the fluorine-assisted dynamic solvothermal method. X-ray diffraction studies indicate the anatase phase of the as-prepared TiO$_2$ (JCPDS No.21-1272) (Figure S7, Supporting Information). Electron microscopy imaging reveals a typical sample size of about 25 nm (Figures S8 and S9, Supporting Information). High-resolution transmission electron microscopy (HRTEM) images were acquired to confirm the different crystal structure between the prepared TiO$_2$ and the crystalline P25 TiO$_2$ (**Figure 2**a,b). In addition, we used a spherical aberration-corrected HRTEM to obtain high-angle annular dark-field (HAADF) image and light-element-sensitive annular bright-field scanning transmission electron microcopy (ABF-STEM) image of the prepared TiO$_2$ (Figure S10a,b, Supporting Information). The structure distortion can be clearly identified in the atomic-resolution image, thereby providing direct evidence of oxygen vacancies in the oxygen-deficient TiO$_2$ (Figure S10c, Supporting Information).[32] Furthermore, X-ray photoelectron spectroscopy (XPS) analysis was performed to measure the electronic states of Ti atoms within the prepared TiO$_2$ (Figures S11 and S12, Supporting Information).[33,34] The spectrum of Ti 2p in prepared TiO$_2$ indicated that the peaks at 458.4 (2p$_{3/2}$) and 464.3 eV (2p$_{1/2}$) come from Ti^{4+}, while the peaks at 457.6 (2p$_{3/2}$) and 463.4 eV (2p$_{1/2}$) arise from Ti^{3+}.[35,36]

The existence of Ti^{3+} was further confirmed by electron energy loss spectroscopy (EELS) and electron paramagnetic resonance (EPR) characterization. EELS test is considered to be powerful to detect the Ti^{3+} in TiO$_2$.[37,38] As shown in Figure 2c, the t$_{2g}$–e$_g$ splitting in L$_3$ is 1.60 eV for the as-synthesized TiO$_2$, which is about 12% narrower than that of P25 (1.81 eV). Meanwhile, the t$_{2g}$–e$_g$ splitting in L$_2$ is 1.21 eV for the as-synthesized TiO$_2$, which is almost 39% narrower than that of P25 (1.99 eV). These results support the presence of Ti^{3+} in the as-formed TiO$_2$. Furthermore, from EPR characterization, as shown in Figure 2d, the strong signal g-values of $g_x = g_y = 1.98$ and $g_z = 1.95$ can be attributed to bulk form Ti^{3+} (Ti$^{3+}_{bulk}$), while the weaker
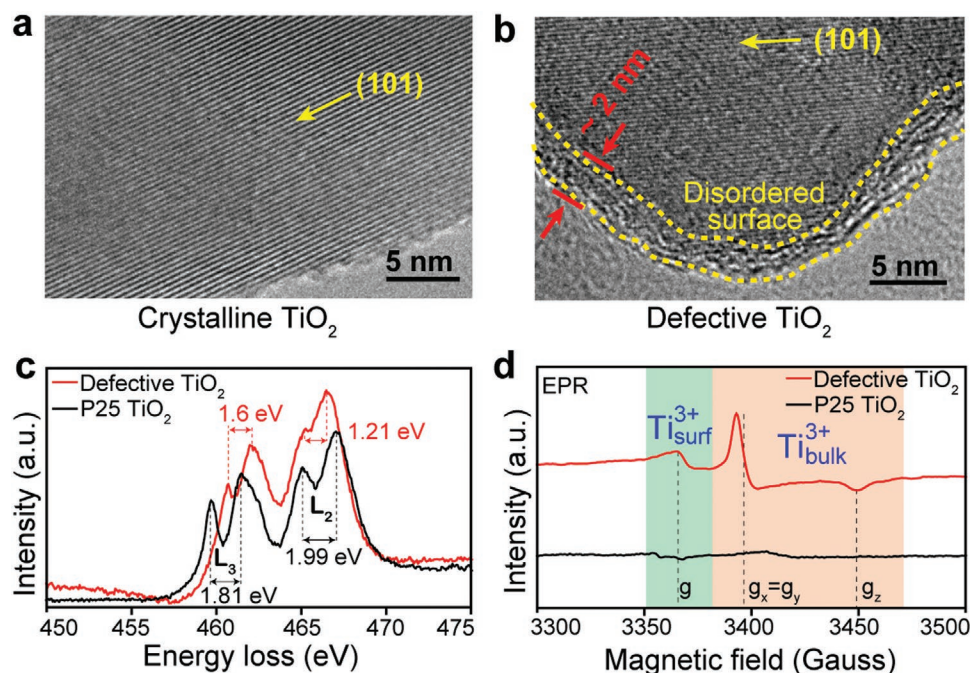
Figure 2. Characterization of the as-synthesized TiO_2 anode materials. a) High-resolution transmission electron microscopy (HRTEM) imaging of crystalline P25 TiO_2. b) HRTEM image of as-synthesized defect-rich TiO_2 material with a 2-nm thickness of disordered surface. c,d) Corresponding electron energy loss spectra and electron paramagnetic resonance spectra of the as-prepared defect-rich TiO_2 sample and crystalline TiO_2 materials.

signal with $g = 2.002$ can be ascribed to surface Ti^{3+} (Ti^{3+}_{surf}).[39,40] By comparison, no marked Ti^{3+} signal was detectable in the crystalline Degussa P25 TiO_2. The concentration of Ti^{3+}_{surf} and Ti^{3+}_{bulk} can be acquired by double integration of the signal area in the EPR spectrum, respectively, and it is worth mentioning that the ratios of bulk-to-surface Ti^{3+} could be readily tuned from 1.0, 1.25, 1.5, 1.75 to 2.0 by controlling the reaction time and the amount of HF during the reaction (Figures S13–S15, Supporting Information). To identify different samples, we labeled the sample with "RX" where X refers to the ratio of bulk-to-surface Ti^{3+}. For example, R1.75 and R2 indicate that the ratio of bulk-to-surface Ti^{3+} is 1.75 and 2, respectively.

To verify the effects of localized electrons on energy storage, we prepared LIBs and NIBs using the as-synthesized TiO_2 materials as anode electrodes and the crystalline P25 TiO_2 as the reference sample.[41,42] Note that large-sized TiO_2 materials, prepared in the absence of HF, are not suitable for control experiments because of their much different ion diffusion length (Figure S16, Supporting Information). Their electrochemical properties were investigated by electrochemical impendence spectroscopy (EIS). **Figure 3**a shows the Nyquist plots of the designed TiO_2 as the anode for LIBs after 15 cycles at 0.5C (1C = 170 mA g^{-1}). The EIS plots of the samples comprise a single semicircle in the high frequency region and a nearly straight line in the low-frequency range, corresponding to the charge transfer resistance (R_{ct}) and solid-state diffusion of lithium (Z_w), respectively.[31] For samples with increasing bulk-to-surface ratios of Ti^{3+} (R1, R1.25, R1.5, R1.75, R2), the R_{ct} value notably decreases from 79.2, 62.3, 59.1, 49.2 to 33.5 Ω, indicating a gradual increase in charge-transfer conductivity. In addition, as the bulk-to-surface ratio of Ti^{3+} increases from 1 to 2, the initial coulomb efficiency increases progressively from 94.7, 96.4, 97.5, 99.5 to 99.7%

(Figure S17, Supporting Information), which matches well with the EIS data. Taken together, the ultrahigh initial columbic efficiency can be attributed to greatly improved charge mobility enabled by Ti^{3+} formation in the anode electrode.

In a further set of experiments, we evaluated the optimal ratio of bulk-to-surface Ti^{3+} for achieving fast energy storage. As shown in Figure 3b, samples were tested from 0.5C, 1C, 2C, 5C, 10C, 20C to 30C and back to 0.5C, with 10 discharge/charge cycles conducted at each current density. It was observed that the samples with localized electrons exhibited significantly improved cycling performance than the commercial P25 control without Ti^{3+}. This clearly suggests that a higher ratio of bulk-to-surface Ti^{3+} can lead to better rate performance. The optimal ratio was determined to be 1.75, for which the highest specific capacity of about 290 mAh g^{-1} was obtained at 0.5C. The specific capacity for P25 was only estimated to be 136 mAh g^{-1}. Although sample R2 shows the best initial performance of EIS and the initial coulombic efficiency, it is inferior than R1.75 in rate performance with only 164 mAh g^{-1} at 0.5C. This should be attributed to the inhibition of ion transport in the presence of two neighboring oxygen vacancies (Figure 1f), which can be validated by measuring the value of ion mobility inside the electrode materials. As expected, the diffusion coefficient of R2 sample is 1.96×10^{-10} cm^2 s^{-1}, much lower than 2.99×10^{-9} cm^2 s^{-1} of R1.75 sample (Figure S18, Supporting Information). In contrast to crystalline TiO_2, the reversible cycling performance of R1.75 can reach a level of 290 mAh g^{-1} at 0.5C and the coulombic efficiency is nearly 100% after 400 cycles (Figure S19, Supporting Information), which shows the state-of-the-art reversible capability among anatase TiO_2-based materials for LIBs (Table S1, Supporting Information).
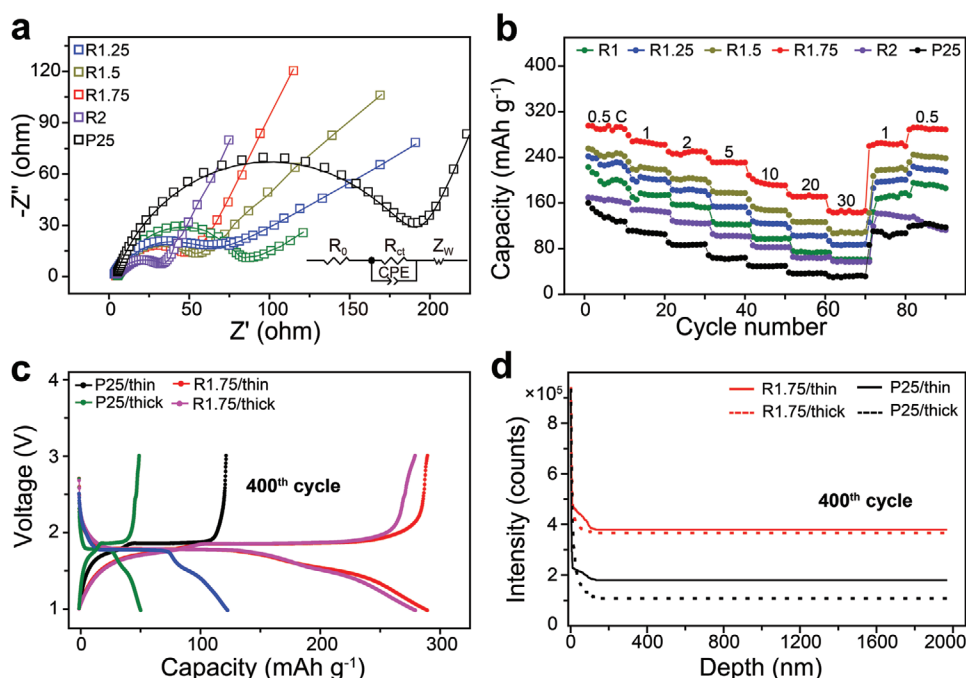
Figure 3. Effects of TiO_2 anode with different localized electrons distribution on electrochemical properties and device performance. a) Electrochemical impendence spectra of the Li-ion battery using localized electrons-containing TiO_2 anode materials and crystalline P25 TiO_2. TiO_2 materials with different amounts of localized electrons (R1.25, R1.5, R1.75, and R2) were investigated by measuring electrochemical impendence spectra. The open symbols and solid lines represent the experimental and simulation results, respectively (inset: equivalent circuit). b) Measurements of specific capacities at various rates (0.5 to 30C) for TiO_2 electrodes with tunable localized electrons distributions. Crystalline TiO_2 electrode was used as a control. c) Galvanostatic discharge–charge curves of the localized electrons-rich TiO_2 electrodes (R1.75) and crystalline TiO_2 electrodes (P25) at a rate of 0.5C in the voltage window of 1.1 to 3.0 V (versus Li/Li⁺). The data were recorded at the 400th cycle. Thin and thick electrodes were tested for the localized electron-rich and crystalline TiO_2 materials, respectively. d) Time-of-flight ion mass spectrometry data recorded for sample R1.75 and crystalline TiO_2 after 400 cycles.

We have also compared the performance of sample R1.75 made in form of a thin (1 mg cm⁻²) or thick (10 mg cm⁻²) electrode layer. The galvanostatic discharge–charge curves (Figure 3c) indicate that the Ti³⁺ rich samples show little difference in terms of performance (290 mAh g⁻¹ vs 279 mAh g⁻¹), while the crystalline P25 samples show a large difference (122 mAh g⁻¹ vs 50 mAh g⁻¹). Moreover, the time-of-flight ion mass spectrometry (ToF-SIMS) measurement in Figure 3d shows that the ion distribution along the in-depth direction in the prepared sample exhibits nearly no degradation in both thick and thin electrodes, while the crystalline TiO_2 target shows considerable degradation. The likely reason is that for thick electrodes, our prepared sample is expected to display much better performance because of the efficiency in ion transport along the depth of the thick electrode. The stability of the oxygen-deficient TiO_2 during electrochemical energy storage was examined by measuring the EPR spectra of R1.75 sample. As shown in Figure S20, Supporting Information, the structure of the prepared samples remained essentially intact after 400 cycles of charging/ discharging operation at 10C.

High-rate energy storage at practical mass loading is critical to the industrial-scale application of electrochemical energy storage. Here, we investigated the high-rate (10C) performance of the designed TiO_2 when used as the electrodes of LIBs and NIBs at practical mass loading (10 mg cm⁻²). As seen in **Figure 4**a,b, for LIBs, our sample R1.75 exhibits a stable specific capacity of 190 mAh g⁻¹ and retains almost 100% after 400 cycles, which is one order of magnitude higher than the specific capacity of the crystalline P25 (17.3 mAh g⁻¹). Meanwhile, for NIBs, sample R1.75 shows a stable specific capacity 142.6 mAh g⁻¹ and nearly no loss after 400 cycles, which is 11 times higher than the specific capacity of the crystalline P25 (11.9 mAh g⁻¹). Cyclic voltammetry results performed on our samples at different scan rates in comparison with the crystalline P25 are shown in Figure 4c–f, and it is obvious that our designed sample shows much enhanced peak current for both LIBs and NIBs. Based on these data, we further carried out ion diffusion calculation. When R1.75 is used for LIBs at a loading of 10 mg, the ion diffusion reaches 2.99×10^{-9} cm² s⁻¹, which is two orders of magnitude larger than that of crystalline P25 (1.45×10^{-11} cm² s⁻¹). Meanwhile, when R1.75 is used for NIBs, the ion diffusion reaches 1.72×10^{-9} cm² s⁻¹, which is also increased by a factor of 100 than that of crystalline P25 (1.05×10^{-11} cm² s⁻¹). Importantly, by virtue of the greatly enhanced ion mobility, the R1.75 shows a reversible high-rate (10C) energy storage of 190 mAh g⁻¹ at a practical mass loading (10 mg cm⁻²), a remarkable performance comparable to a recent work (specific capacity: 152 mAh g⁻¹ at a mass loading of 11 mg cm⁻² at 10C).[4]

Next, we calculated the individual contribution of battery and capacitance capacities based on cyclic voltammetry (CV) measurements using Na-ion battery as an example (Figure S21,
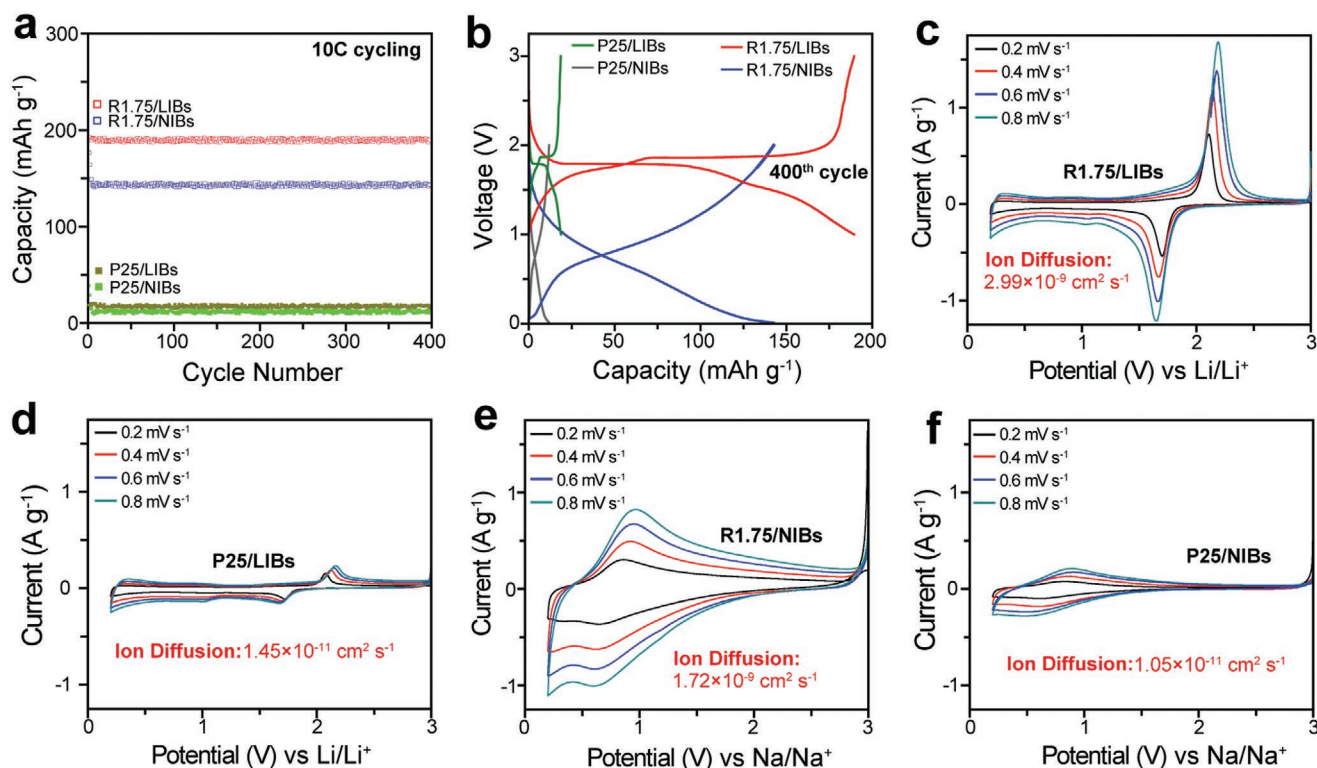
Figure 4. Performance metrics of localized electron-rich TiO$_2$ electrodes with high-rate ion mobility and energy storage. a) High cycling performance of the localized electrons-rich R1.75 TiO$_2$ materials for Li-ion batteries (LIBs) and Na-ion batteries (NIBs) as compared to crystalline P25 TiO$_2$ as the anode material. The data were recorded at 10C and a mass loading of 10 mg cm^{-2}. b) 400th cycle of galvanostatic discharge–charge curves of the LIBs and NIBs recorded for localized electrons-rich R1.75 and crystalline P25 TiO$_2$ as anode materials. c–f) Cyclic voltammograms of electrochemical energy storage from 0.2 to 0.8 mV s^{-1}. The rate capability was measured through the use of localized electrons-rich R1.75 TiO$_2$ for LIBs (c), crystalline P25 TiO$_2$ for LIBs (d), localized electrons-rich R1.75 TiO$_2$ for NIBs (e), and crystalline P25 TiO$_2$ for NIBs (f), respectively. The data were recorded at a scan rate range of 0.2–3 V voltage with a mass loading of 10 mg. Each value of ion diffusion was calculated according to its respective current peak.

Supporting Information). At a scanning rate of 0.2 mV s^{-1}, the capacitance capacity occupies 38.11% for P25 TiO$_2$ and 44.63% ratio for R1.75 TiO$_2$, respectively (Figure S21a,c, Supporting Information). At a high scanning rate of 0.8 mV s^{-1}, the capacitance capacity occupies 55.66% for P25 TiO$_2$ and 61.20% for R1.75 TiO$_2$, respectively (Figure S21b,d, Supporting Information). We found that, in both cases, the capacitance capacity for R1.75 TiO$_2$ accounts for only about 6% increase of their capacitance rate as compared with that for P25 TiO$_2$. A summary of the capacitance rate for P25- and R1.75-based NIBs and LIBs is provided in Figure S21e,f, Supporting Information. With increases in scanning rate from 0.2 to 0.8 mV s^{-1}, the capacitance rate exhibited a small increase of about 7% for these two LIB and NIB samples. Thus, the improvement of rate performance should be enabled by the increased battery capacity through the use of Ti^{3+} enhanced ion transport rather than the capacitance capacity.

Although our prepared defective samples and the widely used P25 TiO$_2$ have the same dimension, the possible affective factors on ion mobility cannot be undoubtedly ruled out. Hence, preparing and comparing two model materials with nearly the same properties except the defect induced Ti^{3+} have been considered. Here, we post-treated the defective TiO$_2$ R1.75 under 450 °C for 8 h in the air and such sample is marked as AR1.75. It is well known that heating the metal oxides under

specific temperature can eliminate the oxygen vacancies, and does not damage their crystal structure and morphology in the meantime. The BET test shows that R1.75 and AR1.75 have similar specific surface areas (33.2 m^2 g^{-1} vs 31.5 m^2 g^{-1}). In addition, they have nearly the same N$_2$ adsorption-desorption curve (Figure S22a, Supporting Information) and the pore size distribution (Figure S22b, Supporting Information). The XRD (Figure S22c, Supporting Information) shows that it is still the anatase phase after treatment. The EPR (Figure S22d, Supporting Information) shows that there is nearly no oxygen-vacancy-related Ti^{3+} signals for AR1.75. Therefore, these two samples R1.75 and AR1.75 can be considered as the nearly perfect models to reveal the influence of oxygen-vacancy-related localized electrons clearly.

Furthermore, the ion mobility test and the Li-ion batteries performances of AR1.75 have been investigated. Based on the CV results (Figure S23a, Supporting Information), the calculated diffusion coefficient of AR1.75 is 1.23 × 10^{-11} cm^2 s^{-1}, which is similar to that of P25 (1.45 × 10^{-11} cm^2 s^{-1}), and is much lower than that of R1.75 (2.99 × 10^{-9} cm^2 s^{-1}). In addition, the Li-ion batteries test (Figure S23b, Supporting Information) shows that the long-term stability performance of AR1.75 at 10C is about 16.9 mAh g^{-1}. This specific capacity is also similar to P25 (17.3 mAh g^{-1}), and is much lower than that of R1.75 (190 mAh g^{-1}). Besides, we have acquired the TEM images of

the R1.75 (Figure S24a, Supporting Information) and AR1.75 (Figure S24b, Supporting Information) under three different states: before, fully charged and after charging/discharging cycles, and it is shown that there is obvious size change for both R1.75 and AR1.75. Hence, after eliminating the possible affecting factors such as crystal sizes and pore distributions, it can be concluded that the superior capacity and ionic mobility can be attributed to the existence of oxygen-vacancy-related Ti^{3+}.

To reveal the fine structural information, the synchrotron radiation X-ray absorption near-edge structure (XANES) and extended X-Ray absorption fine structure (EXAFS) of R1.75 and AR1.75 are acquired. For Ti K-edge XANES (Figure S25, Supporting Information), the spectral profiles of R1.75 and AR1.75 are similar but the former exhibits less intense oscillation, which results from the increased disorder. The main peak locations are nearly the same at about 4987 eV, consistent with the reported anatase works.[43,44] For R1.75, there is obviously lower main peak intensity, which indicates the less unoccupied states because of the rich oxygen vacancies. The absorption edge is shifted to the lower energy, so there should exist lower valence states than Ti^{4+} state,[45] consistent with our EELS and XPS Ti 2p results.

For Ti K-edge EXAFS spectra (Figure S26, Supporting Information), the spectral profiles of R1.75 and AR1.75 are also similar while the intensity of R1.75 is lower. To look into bonding situation, the Ti—O bond and Ti—Ti bond lengths and coordination numbers are extracted and from EXAFS curve fitting (Table S2, Supporting Information). Compared with AR1.75, the R-1.75 with abundant oxygen vacancies possesses a smaller coordination numbers of Ti—O bond (5.9 versus 4.9). The coordination numbers of Ti—Ti bonds are also smaller because the absence of oxygen atoms at specific locations can induce increased disorder. There is no big difference for the bond lengths between R1.75 and AR1.75, which is consistent with the DFT calculated results (Figure S27, Supporting Information).

To investigate whether our prepared material can be well applied for the full-cell batteries, we prepared and tested the tested Na-ion full batteries based on the R1.75 electrode. The retention result (Figure S28, Supporting Information) shows that there is still good performance about 165 mAh g^{-1} after 50 cycles at 5C and a mass loading of 5 mg cm^{-2}. For comparison, sample R1.75 shows a stable specific capacity 142.6 mAh g^{-1} at 10C and a mass loading of 10 mg cm^{-2} in half-cell NIBs (Figure 4a). Thus, the prepared sample R1.75 can show good capacity performance in both half and full batteries.

The schematic in Figure S29, Supporting Information, shows how enhanced ion transport results in the high mass loading electrode obtained by comparing the Ti^{3+}-rich TiO_2 sample with its crystalline counterpart. In stacked crystalline TiO_2 sample, the ions always react with electrons at the sub-surface under a high rate on account of limited ion transport, thus inhibiting ion intercalation at a deeper level. By comparison, the LIT effect enables ion transport in TiO_2 sample with localized electrons to be carried through two pathways: direct intercalation and interfacial diffusion. The ions can be easily transported deeply into stacked TiO_2 sample because of high ion conduction and facile interfacial ion diffusion. Taken together, these results unambiguously suggest that an optimal distribution of Ti^{3+} within TiO_2 materials can greatly enhance the process of ion transport through electrodes with high mass loading, which is critical for high-rate energy storage.

The localized electron-assisted LIT mechanism in this experiment allows significant promotion of ion mobility inside the electrode materials for ultrafast electrochemical energy storage. First-principle calculations reveal that localized electrons can be introduced by defect engineering, and the migration barrier of Li^+ is only 0.53 eV, about 0.1 eV lower than the perfect structure. After considering the external electric field, the migration barrier in samples with localized electrons can further decrease by 0.16 eV. Consistent with the theory calculation results, the LIT mechanism leads to the enhanced Li^+ and Na^+ diffusivity by two orders of magnitude. At high mass loading of 10 mg cm^{-2} and high rate of 10C, a reversible energy storage capacity up to 190 mAh g^{-1} is achieved, which is ten times greater than achievable by commercial crystals with comparable dimensions. The observation of the LIT effect opens a new route to implementing high-rate electrochemical energy storage at practical mass loading.

Experimental Section

Materials Synthesis: All of the chemical reagents of analytical grade were purchased from Shanghai Aladdin Bio-Chem Technology Co. and used as received without further purification. The P25 TiO_2 was purchased from Degussa (the size: 25 nm, 80% anatase/20% rutile phase). In a typical experiment, 1 mL of aqueous TBOT precursor was dissolved in 25 mL of *n*-propanol and then 0.8 mL of HF were added to the mixed solution. The resulting suspension was subsequently transferred to a Telfon-lined stainless steel autoclave and then heated at 160 °C for 24 h. After the reaction, the reaction product was washed with deionized water, and then was washed with ethanol and deionized water. The reaction of synthesizing TiO_2 with different defect concentration and distribution mainly consists of three processes, including decomposition, nucleation, and growth (Figure S8, Supporting Information). Note that a high amount of F^- will promote the formation of bulk Ti^{3+}, while a long reaction time favors the formation of surface Ti^{3+}. To identify different samples, we labeled the sample with "RX" where X refers to the ratio of bulk-to-surface Ti^{3+}. This ratio was calculated based on the EPR data. The specific post-treated TiO_2 under 450 °C for 8 h in the air is marked as ARX, such as AR1.75. Details for material characterization, electrochemical measurements, theoretical calculation, and calculation of the diffusion coefficients of positive ions are given in Supporting Information

Supporting Information

Supporting Information is available from the Wiley Online Library or from the author.

Acknowledgements

Conflict of Interest

The authors declare no conflict of interest.

Keywords

[1] H. M. Cheng, F. Li, *Science* **2017**, *356*, 582.

[2] J. Liang, F. Li, H. M. Cheng, *Energy Storage Mater.* **2017**, *6*, A1.

[3] Y. Gogotsi, P. Simon, *Science* **2011**, *334*, 917.

[4] H. T. Sun, L. Mei, J. F Liang, Z. P. Zhao, C. Lee, H. L. Fei, M. N. Ding, J. Lau, M. F. Li, C. Wang, X. Xu, G. L. Hao, B. Papandrea, I. Shakir, B. Dunn, Y. Huang, X. F. Duan, *Science* **2017**, *356*, 599.

[5] C. S. Rustomji, Y. Yang, T. K. Kim, J. Mac, Y. J. Kim, E. Caldwell, H. Chung, Y. S. Meng, *Science* **2017**, *356*, 1351.

[6] N. N. Wang, Z. C. Bai, Y. T. Qian, J. Yang, *Adv. Mater.* **2016**, *28*, 4126.

[7] A. Van der Ven, J. Bhattacharya, A. A. Belak, *Acc. Chem. Res.* **2012**, *46*, 1216.

[8] M. Park, X. Zhang, M. Chung, G. B. Less, A. M. Sastry, *J. Power Sources* **2010**, *195*, 7904.

[9] K. Kang, Y. S. Meng, J. Bréger, C. P. Grey, G. Ceder, *Science* **2006**, *311*, 977.

[10] J. Chen, W. X. Song, H. S. Hou, Y. Zhang, M. J. Jing, X. N. Jia, X. B. Ji, *Adv. Funct. Mater.* **2015**, *25*, 6793.

[11] M. Odziomek, F. Chaput, A. Rutkowska, K. Świerczek, D. Olszewska, M. Sitarz, F. Lerouge, S. Parola, *Nat. Commun.* **2017**, *8*, 15636.

[12] Y. Tang, Y. Zhang, W. Li, B. Ma, X. Chen, *Chem. Soc. Rev.* **2015**, *44*, 5926.

[13] P. Bottke, Y. Ren, I. Hanzu, P. G. Bruce, M. Wilkening, *Phys. Chem. Chem. Phys.* **2014**, *16*, 1894.

[14] L. R. De Jesus, G. A. Horrocks, Y. F. Liang, A. Parija, C. Jaye, L. Wangoh, J. Wang, D. A. Fischer, L. F. J. Piper, D. Prendergast, S. Banerjee, *Nat. Commun.* **2016**, *7*, 12022.

[15] B. Ellis, L. K. Perry, D. H. Ryan, L. Nazar, *J. Am. Chem. Soc.* **2006**, *128*, 11416.

[16] M. Setvin, C. Franchini, X. F. Hao, M. Schmid, A. Janotti, M. Kaltak, C. G. Van de Walle, G. Kresse, U. Diebold, *Phys. Rev. Lett.* **2014**, *113*, 086402.

[17] F. D. Angelis, C. D. Valentin, S. Fantacci, A. Vittadini, A. Selloni, *Chem. Rev.* **2014**, *114*, 9708.

[18] C. Franchini, G. Kresse, R. Podloucky, *Phys. Rev. Lett.* **2009**, *102*, 256402.

[19] B. J. Morgan, G. W. Watson, *Phys. Rev. B* **2009**, *80*, 233102.

[20] M. Gerosa, C. E. Bottani, L. Caramella, G. Onida, C. D. Valentin, G. Pacchioni, *J. Chem. Phys.* **2015**, *143*, 134702.

[21] S. Q. Wu, X. J. Tan, J. Y. Lei, H. J. Chen, L. Z. Wang, J. L. Zhang. *J. Am. Chem. Soc.* **2019**, *141*, 6592.

[22] Z. W. Seh, W. Y. Li, J. J. Cha, G. Y. Zheng, Y. Yang, M. T. McDowell, P. Hsu, Y. Cui, *Nat. Commun.* **2013**, *4*, 1331.

[23] S. Li, J. J. Niu, Y. C. Zhao, K. P. So, C. Wang, C. A. Wang, J. Li, *Nat. Commun.* **2015**, *6*, 7872.

[24] H. T. Fang, M. Liu, D. W. Wang, T. Sun, D. S. Guan, F. Li, J. G. Zhou, T. K. Sham, H. M. Cheng, *Nanotechnology* **2009**, *20*, 225701.

[25] H. Park, T. Song, H. Han, A. Devadoss, J. Yuh, C. Choi, U. Paik, *Electrochem. Commun.* **2012**, *22*, 81.

[26] J. Osorio-Guillén, S. Lany, A. Zunger, *Phys. Rev. Lett.* **2008**, *100*, 036601.

[27] G. L. Miessler, D. A. Tarr, *Inorganic Chemistry*, Prentice-Hall: Upper Saddle River, NJ, USA **1999**.

[28] R. Sanjinés, H. Tang, H. Berger, F. Gozzo, G. Margaritondo, F. Lévy, *J. Appl. Phys.* **1994**, *75*, 2945.

[29] A. G. Thomas, W. R. Flavell, A. R. Kumarasinghe, A. K. Mallick, D. Tsoutsou, G. C. Smith, R. Stockbauer, S. Patel, M. Grätzel, R. Hengerer. *Phys. Rev. B* **2003**, *67*, 035110.

[30] S. Q. Zhou, E. Čižmár, K. Potzger, M. Krause, G. Talut, M. Helm, J. Fassbender, S. A. Zvyagin, J. Wosnitza, H. Schmidt, *Phys. Rev. B* **2009**, *79*, 113201.

[31] S. Yang, L. E. Halliburton, A. Manivannan, P. H. Bunton, D. B. Baker, M. Klemm, S. Horn, A. Fujishima, *Appl. Phys. Lett.* **2009**, *94*, 162114.

[32] Y. Q. Yang, L. C. Yin, Y. Gong, P. Niu, J. Q. Wang, L. Gu, X. Q. Chen, G. Liu, L. Z. Wang, H. M. Cheng, *Adv. Mater.* **2018**, *6*, 1704479.

[33] J. C. Yu, J. Yu, W. Ho, Z. Jiang, L. Zhang, *Chem. Mater.* **2002**, *14*, 3808.

[34] T. R. Gordon, M. Cargnello, T. Paik, F. Mangolini, R. T. Weber, P. Fornasiero, C. B. Murray, *J. Am. Chem. Soc.* **2012**, *134*, 6751.

[35] H. Cui, W. Zhao, C. Y. Yan, H. Yin, T. Q. Lin, Y. F. Shan, Y. Xie, H. Gu, F. Q. Huang, *J. Mater. Chem. A* **2014**, *2*, 8612.

[36] J. J. Xu, D. Wang, H. L. Yao, K. J. Bu, J. Pan, J. Q. He, F. F. Xu, Z. L. Hong, X. B. Chen, F. Q. Huang, *Adv. Mater.* **2018**, *10*, 1706240.

[37] A. Naldoni, M. Allieta, S. Santangelo, M. Marelli, F. Fabbri, S. Cappelli, C. L. Bianchi, R. Psaro, V. D. Santo, *J. Am. Chem. Soc.* **2012**, *134*, 7600.

[38] L. D. Li, J. Q. Yan, T. Wang, Z. J. Zhao, J. Zhang, J. L. Gong, N. J. Guan, *Nat. Commun.* **2015**, *6*, 5881.

[39] F. Zuo, L. Wang, T. Wu, Z. Y. Zhang, D. Borchardt, P. Y. Feng, *J. Am. Chem. Soc.* **2010**, *132*, 11856.

[40] J. W. Chen, G. X. Wu, T. Y. Wang, X. D. Li, M. C. Li, Y. H. Sang, H. Liu, *ACS Appl. Mater. Interfaces* **2017**, *9*, 4634.

[41] G. Kim, C. Jo, W. Kim, J. Chun, S. Yoon, J. Lee, W. Choi, *Energy Environ. Sci.* **2013**, *6*, 2932.

[42] H. Ren, R. Yu, J. Wang, Q. Jin, M. Yang, D. Mao, D. Kisailus, H. Zhao, D. Wang, *Nano Lett.* **2014**, *14*, 6679.

[43] Y. Q. Yang, L. C. Yin, Y. Gong, P. Niu, J. Q. Wang, L. Gu, X. Q. Chen, G. Liu, L. Z. Wang, H. M. Cheng, *Adv. Mater.* **2018**, *30*, 1704479.

[44] W. Zhou, W. Li, J. Q. Wang, Y. Qu, Y. Yang, Y. Xie, K. F. Zhang, L. Wang, H. G. Fu, D. Y. Zhao, *J. Am. Chem. Soc.* **2014**, *136*, 9280.

[45] S. S. Huang, Y. H. Lin, W. Chuang, P. S. Shao, C. H. Chuang, J. F. Lee, M. L. Lu, Y. T. Weng, N. L. Wu, *ACS Sustainable Chem. Eng.* **2018**, *6*, 3162.